

# Regression is all you need for medical image translation

Sebastian Rassmann, David Kügler, Christian Ewert, Martin Reuter

**Abstract**—The acquisition of information-rich images within a limited time budget is crucial in medical imaging. Medical image translation (MIT) can help enhance and supplement existing datasets by generating synthetic images from acquired data. While Generative Adversarial Nets (GANs) and Diffusion Models (DMs) have achieved remarkable success in natural image generation, their benefits – creativity and image realism – do not necessarily transfer to medical applications where highly accurate anatomical information is required. In fact, the imitation of acquisition noise or content hallucination hinder clinical utility. Here, we introduce *YODA* (You Only Denoise once - or Average), a novel 2.5D diffusion-based framework for volumetric MIT. *YODA* unites diffusion and regression paradigms to produce realistic or noise-free outputs. Furthermore, we propose Expectation-Approximation (ExpA) DM sampling, which draws inspiration from MRI signal averaging. ExpA-sampling suppresses generated noise and, thus, eliminates noise from biasing the evaluation of image quality. Through extensive experiments on four diverse multi-modal datasets – comprising multi-contrast brain MRI and pelvic MRI-CT – we show that diffusion and regression sampling yield similar results in practice. As such, the computational overhead of diffusion sampling does not provide systematic benefits in medical information translation. Building on these insights, we demonstrate that *YODA* outperforms several state-of-the-art GAN and DM methods. Notably, *YODA*-generated images are shown to be interchangeable with, or even superior to, physical acquisitions for several downstream tasks. Our findings challenge the presumed advantages of DMs in MIT and pave the way for the practical application of MIT in medical imaging.

**Index Terms**—generative diffusion models, medical image translation, white-matter hyper-intensities, innovation bias

## I. INTRODUCTION

The capabilities of learning complex, multi-modal distributions have made Generative Adversarial Nets (GANs) [1], [2] and, moreover, Diffusion Models (DMs) [3]–[5] some of the dominant design principles for natural image generation tasks. Both types of models excel at generating realistic-appearing

This work was supported by the German BMBF (031L0206), the NIH (R01MH131586, R01MH130899, R01AG064027), the CZI (EOSS5 2022-252594), and the Helmholtz Foundation Model Initiative (Human Radiome Project). We thank the Rhineland Study for providing data and WMH annotations.

All authors are with the German Center for Neurodegenerative Diseases (DZNE), Bonn, Germany (e-mail: sebastian.rassmann@dzne.de, david.kuegler@dzne.de, christian.ewert@dzne.de, martin.reuter@dzne.de). Martin Reuter is additionally with the A.A. Martinos Center for Biomedical Imaging, Boston, MA, USA and the Department of Radiology, Harvard Medical School, Boston, MA, USA.

textures and achieve visually ever more pleasing images [6]–[10]. This success has also fostered their application for medical image generation [11], [12]. In particular, generating synthetic, complementary target from acquired source modalities in medical image translation (MIT) may be leveraged to expand or improve existing datasets, or to accelerate multi-modal imaging protocols by eliminating redundant acquisitions and thereby reducing acquisition time. An example in brain magnetic resonance (MR) imaging is the acquisition of T2 fluid-attenuated inversion recovery (FLAIR). Although it is popular for detecting lesions such as white matter hyperintensities (WMHs), a biomarker for several neurological morbidities [13], [14], the acquisition of FLAIR is slow due to the inversion recovery and, therefore, FLAIR is often acquired at lower resolutions [15]–[17] or omitted altogether [18]. Due to this practical utility, MIT is a promising and active research field with a focus on GANs [19]–[24] and DMs [25]–[33]. Specifically, recent work shows superior performance for DMs, which is often attributed to their explicit likelihood estimation [25], [26] and iterative image refinement during image generation [25]. Furthermore, non-deterministic DM sampling is highlighted for estimating uncertainty [32], [34]. Yet, there is an important difference between image-to-image (I2I) tasks for medical and natural images: Whereas natural image generation aims to generate realistic and pleasing images, medical images are obtained for the information contained in them, which is ultimately visually inspected or automatically extracted in downstream applications. Thus, the perceptual quality and realism of medical images are irrelevant as long as relevant medical information such as biomarkers or pathologies are contained. In addition, noise is a common problem during acquisition generating fine-grained details in medical images [35]–[37]. Whereas GANs’ and DMs’ popularity and success can be attributed to the generation of low-level features to create realistic images [6], [9], in MIT, this implies either replicating acquisition noise or hallucinating about – potentially false – medical information. While deliberately generating noisy images is, in general, already undesirable and opposes efforts of noise suppression during image acquisition [16], [35], hallucinating about relevant medical information can even lead to misinterpretation or wrong diagnoses. MIT, and modality translation in particular, should therefore optimize the preservation of information, i.e., minimize image distortion rather than improve perceptual quality [38] avoiding hallucination and facilitating downstream analyses by noise suppression.

In contrast to DMs and GANs, Regression Models (RMs) are

trained with pixel-wise regression losses (also called minimum mean-squared-error models). They approximate the expected value in their respective tasks rather than sampling from probability distributions like DMs and GANs, i.e. by design, RMs do not replicate non-deterministic image features like noise [39]. However, the resulting blurriness and reduced perceptual quality [2], [6], [9], [38], [40]–[42] may constitute a domain shift with respect to (w.r.t.) real images and is suggested to hamper diagnostics [34].

Here, we systematically compare RMs and DMs for MIT. To this end, we propose *YODA*, a 2.5D DM operating in the uncompressed pixel space as a multi-purpose approach to volumetric medical I2I tasks. While *YODA* is designed and trained as a DM, it allows for RM-like sampling by simply using the initial target image prediction without further refinement. In addition, we introduce expectation-approximation (ExpA) sampling: Inspired by the physical paragon in MR imaging, we exploit the probabilistic nature of DMs to generate and average multiple images to eliminate noise. Thus, ExpA sampling allows us to mitigate the perception-distortion tradeoff [38]. To ultimately assess image distortion, i.e. accuracy in translating medically relevant information in the images, and to test the actual practical suitability of the generated images, we extend common evaluation frameworks by assessing relevant downstream tasks. We find no evidence for systematically superior performance of DMs over RMs in extensive experiments with four large datasets: the Rhineland Study (RS) [16], BraTS [17], [43], [44] and IXI for multi-contrast brain MRI, as well as the Gold atlas comprising pelvic MRI and CT [45]. Furthermore, we note that the higher perceptual quality of DMs is largely governed by the imitation of noise. This implies that, for the application of MIT, DMs only consume computational resources to simulate acquisition noise, whereas noise-free images, which are preferable for most applications, can be obtained much more efficiently. In addition, our findings question the application of DMs for uncertainty estimation if noise imitation dominates the divergence of diffusion trajectories. Using these insights, we demonstrate the vast superiority of regression-sampled *YODA* over several strong GAN [20], [21] and DM baselines [25]–[27]. Finally, we show that our synthetic images are largely interchangeable with the acquired images in the assessed downstream tasks and that the learned translation generalizes to unseen datasets.

### Contributions

Thus, our contributions summarize as follows:

- We establish *YODA* as a novel 2.5D diffusion approach for MIT. We address and leverage the volumetric nature of MR images fostering 3D coherency while maintaining computational traceability of uncompressed DMs.
- Based on analytical and empirical observations of the effects of noise in the generation and evaluation of synthetic images, we introduce ExpA sampling to systematically compare diffusion and regression paradigms. Using these insights we demonstrate the practical equivalence of diffusion and regression sampling.
- We show the superiority of *YODA*'s image generation quality over several strong baselines on four different

datasets including MRI and CT, asserting the suitability of the generated images for downstream tasks and the generalization to external data.

We publish the models at [github.com/Deep-MI/YODA](https://github.com/Deep-MI/YODA).

## II. RELATED WORK

Approaches based on conditional GANs (cGANs) [1], [2] have long dominated MIT [19]–[21], [23], [24]. The initial work on 2D cGANs [19] was subsequently extended by ResViT [20] and Ea-GANs [21]. ResViT introduces residual transformer blocks for the generator [20], whereas Ea-GANs conduct MIT in 3D and add edge information to the GAN loss [21]. Ea-GAN has also shown promising results for deriving FLAIR from diffusion-weighted images [22]. Recently, DMs [3]–[5] were established as state-of-the-art for various natural image generation tasks [8]–[10], [41]. DMs operate through many (typically  $T \geq 1000$ ) latent images with in- or decreasing levels of noise. While the forward diffusion process gradually adds noise, the generative backward process iteratively recovers the images using a trained neural network. Thus, the trained network can generate realistic images from pure noise. Yet, DM's iterative nature demands a high number of function evaluations ( $N_{FE}$ ). The resulting high computational costs are exacerbated by the 3D nature of most medical image modalities. Still, DMs were widely adopted for MIT tasks [25]–[33]. The pioneering work of Özbey et al. proposes *SynDiff*, an adversarial DM, for unpaired MIT [25]. The authors added GAN losses to compensate for larger denoising steps, reducing the required  $N_{FE}$ . To a similar effect, *FastDDPM* introduces an accelerated sampling scheme [31]. However, we find that accelerated DM sampling reduces high-frequency details (see also the figures in [31]). As we show in Sec. III-A and IV-A, this effect biases the reported metrics for image quality, as perceptual quality is traded for reduced distortion [38].

A variant of DMs for I2I tasks is diffusion bridges (DBs) [46], [47]. DBs use the conditioning images rather than noise as a prior for the generative diffusion process, which can result in a more direct sampling path [46], [47]. DBs have therefore gained popularity for MIT [26], [29], [32], [34]. An example is the adversarial DM *SelfRDB* [26] which introduced a self-consistency step during sampling, i.e. editing the image until convergence to improve generation accuracy. CMDM [32] uses a dedicated GAN to generate the DB's prior and additionally employs a multi-path shortcut diffusion strategy, i.e., multiple predictions of the DM are averaged to increase translation accuracy and estimate the prediction uncertainty [32]. To address the challenge of consistency of 3D images in MIT, Choo et al. [29] recently proposed sampling their 2D slab-based DB using a novel inter-slice trajectory alignment that averages several overlapping predictions.

Whereas uncompressed 3D DMs are currently impractical for full-resolution image synthesis due to hardware constraints [48], a feasible 3D design choice is latent DMs (LDMs) [10], [49]. Here, DMs operate in the latent space of separately pre-trained autoencoders to reduce the memory footprints. Hence, full-resolution 3D LDMs are realizable on current hardware

[27], [33], [50], with the notable example of ALDM [27] that combines the DMs with latent SPADE blocks and shows promising results for MR contrast translation.

Despite findings that simple RMs can effectively learn expectation values of images even if trained solely on noisy samples [39], RMs were rarely considered for MIT, and synthesis results of RMs lacked even anatomically well-defined details such as the gray-white matter (GM/WM) contrast [40] or were only applied to small, private datasets and relatively simple tasks [51].

For I2I tasks on natural images, the evaluation of several early DMs considered training the neural denoiser as RMs baselines [9], [41], [42]. This revealed that DMs trade distortion (SSIM and PSNR) for perceptual quality (e.g. Fréchet inception distance, FID, [52] or human preference [9], [41]) owing e.g. to the ability to hallucinate high-frequency details [9], [41], [42]. Whereas ablations of the diffusion process were conducted for ALDM [27], using the neural backbone as a simple RM baseline is commonly omitted [25], [26], [28]–[32]. The recent work on medical image denoising showed that single-shot regression sampling of DMs reduces image distortion in comparison to native DM sampling [53].

### III. METHODS

#### A. Acquisition noise in quality evaluation

To illustrate the bias of image metrics for evaluating MIT with noisy images, we analyze its theoretical implications. Modeling MR acquisition as a complex-valued probabilistic process [36], [37], the MR magnitude image  $X$  is the combination of a hypothetical, “true” image  $X'$  and the complex-valued (primarily thermal acquisition) noise  $n_{\text{Re}} + i \cdot n_{\text{Im}}$ :

$$X = |X' + n_{\text{Re}} + i \cdot n_{\text{Im}}|, \quad n_{\text{Re}}, n_{\text{Im}} \sim \mathcal{N}(0, \sigma^2 \mathbf{I}). \quad (1)$$

Note, however, that this disregards important non-Rician corruptions, e.g. due to accelerated acquisition or motion [37]. Acquiring and averaging  $N_{\text{Ex}} \gg 1$  independent images suppresses the noise ( $\sigma \propto 1/\sqrt{N_{\text{Ex}}}$ ) and, in theory, allows us to approximate the noise-free image  $X'$ :

$$\lim_{N_{\text{Ex}} \rightarrow \infty} \bar{X}_{N_{\text{Ex}}} = \lim_{N_{\text{Ex}} \rightarrow \infty} \text{RMS}(X_1, \dots, X_{N_{\text{Ex}}}) = X'. \quad (2)$$

However, assuming a sufficient SNR  $\geq 2$ , we simplify the Rician to Gaussian noise [36], [37], i.e.  $X \sim \mathcal{N}(X', \sigma^2 \mathbf{I})$ .

When training GANs and DMs with acquired images  $X \sim \mathcal{X}$ , sampling the DM  $p_\theta$  results in “noisy” images, as they aim to maximize the likelihood of a generated image  $\hat{X} \sim p_\theta$  w.r.t.  $\mathcal{X}$ . Yet, noise replication influences the assessed image quality: Modeling the generated images  $\hat{X}$  analogously to the acquisition as  $\hat{X}_{\hat{\sigma}} \sim \mathcal{N}(\hat{X}', \hat{\sigma}^2 \mathbf{I})$  the MSE decomposes to:

$$\begin{aligned} \text{MSE}(\hat{X}_{\hat{\sigma}}, X) &= \underbrace{\mathbb{E}[\Delta X'^T \Delta X']}_{=\text{MSE}(\hat{X}', X')} + \underbrace{\mathbb{E}[n^T n]}_{=\sigma^2} + \underbrace{\mathbb{E}[\hat{n}^T \hat{n}]}_{=\hat{\sigma}^2} - \underbrace{2\mathbb{E}[n^T \hat{n}]}_{=0} \\ \hat{X}_{\hat{\sigma}} \sim p_\theta & \\ X \sim \mathcal{X} & \end{aligned} \quad \begin{array}{l} \text{(Acq. noise)} \\ \text{(Gen. noise)} \end{array}$$

The noise  $n$  is random by definition and, therefore, unrecoverable and not correlated with  $\hat{n}$  ( $\mathbb{E}[n^T \hat{n}] = 0$ ). Thus, the MSE and the derived PSNR penalize noise creation, favoring solutions with small  $\hat{\sigma}$ . Similar observations can be made for the SSIM. Conversely, reduced  $\hat{\sigma}$  is unrealistic and, therefore,

impairs the perceptual quality. Hence, the noise amplitude  $\hat{\sigma}$  determines the well-described trade-off between perceptual quality and image distortion, i.e. image realism vs. faithful and accurate generation of synthetic images [38].

#### B. YODA

YODA is based on the foundational design of DDPMs [5]. The forward process uses the noise schedule  $\beta_t$  for  $t \in [1, T]$ :

$$q(X_t | X_{t-1}) \sim \mathcal{N}\left(\sqrt{1 - \beta_t} X_{t-1}, \beta_t \mathbf{I}\right). \quad (3)$$

With  $\bar{\alpha}_t = \prod_{s=1}^t (1 - \beta_s)$ , this results in latent images

$$X_t = \sqrt{\bar{\alpha}_t} X_0 + \sqrt{1 - \bar{\alpha}_t} \varepsilon, \quad \varepsilon \sim \mathcal{N}(0, \mathbf{I}). \quad (4)$$

Conversely, the generative backward process follows

$$q(X_{t-1} | X_t) = \int_{X_0} q(X_{t-1} | X_t, X_0) q(X_0 | X_t) dX_0 \quad (5)$$

with  $q(X_{t-1} | X_t, X_0)$  from the forward process (3) and  $q(X_0 | X_t)$  incorporates knowledge of the data distribution  $\mathcal{X}$ . In practice, the image  $\hat{X}_0$  is approximated iteratively by predicting the acquired image ( $\hat{X}_{t \rightarrow 0} \approx X_0$ ) at each time step  $t$  using a trained neural network  $p_\theta$  as

$$p_\theta(\hat{X}_{t-1} | \hat{X}_t) = \sqrt{\bar{\alpha}_t} \hat{X}_{t \rightarrow 0} + \sqrt{1 - \bar{\alpha}_t} \varepsilon_t \rightarrow \hat{X}_{t-1} \quad (6)$$

with an initial starting value  $\hat{X}_T \sim \mathcal{N}(0, \mathbf{I})$ .

Whereas DMs usually predict either the noise-free image  $X_0$  or the noise  $\varepsilon_t$ , YODA predicts the velocity  $v_t = \sqrt{\bar{\alpha}_t} \varepsilon - \sqrt{1 - \bar{\alpha}_t} X_0$  [54]. Derived from the evidence lower bound of the probabilistic model [5], the training objective for  $v_\theta$  is the empirical risk minimization of the velocity differences

$$\min_{\theta} \mathbb{E}_{(X_0, C) \sim \mathcal{X}_C, \varepsilon \sim \mathcal{N}(0, \mathbf{I}), t \sim \mathcal{U}_T} [L_2(v_\theta(X_t, t, C), v_t)], \quad (7)$$

where  $\mathcal{X}_C$  denotes the distribution of source-target image pairs and  $\mathcal{U}_T$  the uniform distribution of time steps. Training and sampling are described in Alg. 1 and 2:

---

#### Algorithm 1 Training YODA

---

```

1: for  $(X, C) \sim \mathcal{X}_C, \varepsilon \sim \mathcal{N}(0, \mathbf{I}), t \sim \mathcal{U}_T$  do
2:    $X_t = \sqrt{\bar{\alpha}_t} X + \sqrt{1 - \bar{\alpha}_t} \varepsilon$  # forward diffusion
3:    $v_t = \sqrt{\bar{\alpha}_t} \varepsilon - \sqrt{1 - \bar{\alpha}_t} X$  #  $v$ -prediction target
4:   Gradient descent step on:  $\nabla_{\theta} L_2(v_\theta(X_t, t, C), v_t)$ 

```

---



---

#### Algorithm 2 Sampling YODA

---

```

Require:  $C$ : conditioning images,  $X_T = \varepsilon_T \sim \mathcal{N}(0, \mathbf{I})$ 
1: for  $t$  in  $\{T, \dots, 1\}$  do #  $\forall$  time steps
2:    $\hat{X}_{t \rightarrow 0} = \sqrt{\bar{\alpha}_t} \hat{X}_t - \sqrt{1 - \bar{\alpha}_t} v_\theta(\hat{X}_t, t, C)$  # prediction
3:   if  $t > 1$  then
4:      $\varepsilon_{t-1} \sim \mathcal{N}(0, \mathbf{I})$  # draw noise
5:      $\hat{X}_{t-1} = \sqrt{\bar{\alpha}_{t-1}} \hat{X}_{t \rightarrow 0} + \sqrt{1 - \bar{\alpha}_{t-1}} \varepsilon_{t-1}$  # re-noise
6: return  $\hat{X}_0 = \hat{X}_{t \rightarrow 0}$ 

```

---

Using the introduced concepts and notation, we describe our modifications of standard DDPMs in the following:

1) **2.5D diffusion:** Operating the neural denoiser on full-resolution 3D images is unfeasible on current hardware due to memory constraints. Thus, we perform a 2.5D diffusion approach: We define the diffusion process in 3D, while operating the denoiser  $v_\theta$  on 2D slices, stacking the output of  $v_\theta$  to form latent diffusion volumes  $\hat{X}_t$ . Based on this, we include the following 2.5D components:

a) *multi-slice inputs*:  $v_\theta$  predicts a single slice from a slab formed with the two bi-directional adjacent slices (i.e. 5 in total) of both, the diffusion latent  $\hat{X}_t$  and the conditioning  $C$ .

b) *orthogonal denoising*: We rotate the slicing views (sagittal, coronal, axial) between denoising steps to improve 3D information transfer and combat slicing artifacts.

2) *Truncated sampling*: As the initial solution  $\hat{X}_{T \rightarrow 0}$  remains practically unchanged for many late diffusion steps, we truncate DM sampling: we skip the following  $\sim 75\%$  low-SNR denoising steps, i.e. we only consider  $t \in \{T, T/4, \dots, 1\}$  in line 1 of Alg. 2. Note that in contrast to CMDM [32], we derive the truncation directly from the backward process, re-using the initial DM solution,  $\hat{X}_{T \rightarrow 0}$ , as the prior.

3) *Expectation-approximation (ExpA) sampling*: DM sampling is non-deterministic due to adding random noise in the backward process ( $\varepsilon_t$  in (6) and Alg. 2). Thus, for each run  $i \in \{1, \dots, N\}$ , the sample  $\hat{X}_{\theta,i} \sim p_\theta$  has a different noise manifestation  $\hat{n}_i$ . We can thus approximate the DM’s expected value analogously to acquisition averages (2) as  $\hat{X}_{\theta, N_{\text{Ex}}} = \text{RMS}(\hat{X}_{\theta,1}, \dots, \hat{X}_{\theta, N_{\text{Ex}}})$ . For a perfect DM (i.e.  $\text{KL}[p_\theta(C) \parallel p(X|C)] = 0$ ), we would obtain

$$\mathbb{E}_{\hat{X} \sim p_\theta(C)} \stackrel{\hat{n}_i \sim \mathcal{N}}{=} \lim_{N_{\text{Ex}} \rightarrow \infty} \hat{X}_{\theta, N_{\text{Ex}}} \stackrel{\text{KL}=0}{=} \lim_{N_{\text{Ex}} \rightarrow \infty} \bar{X}_{N_{\text{Ex}}} \stackrel{(2)}{=} X'. \quad (8)$$

4) *Efficient approximation of expected values*: Let us now investigate the behavior of DMs for the first denoising iteration, i.e.  $t=T$ , in more detail. Since  $\bar{\alpha}_T \approx 0$ , DMs receive pure, uninformative noise  $\varepsilon$  as the diffusion prior. Denoting the joint distribution of noise-free targets and conditions as  $\mathcal{X}'_C$ , the training objective at  $t=T$  simplifies to:

$$\min_{\theta} \mathbb{E}_{(X', C) \sim \mathcal{X}'_C, n \sim \mathcal{N}(0, \sigma^2 \mathbf{I})} [L_2(v_\theta(C), |X' + n|)]. \quad (9)$$

The theoretical minimum of this objective is assumed for  $\hat{X}_{T \rightarrow 0} = \mathbb{E}[X] = X'$ , i.e. a perfect DM would already predict noise-free images in the first sampling operation. This provides a tractable alternative to sampling the DM with  $N_{\text{Ex}} = \infty$ . We therefore also considered this initial solution of *YODA* as a sampling method for approximating noise-free images, i.e.  $\hat{X}_{T \rightarrow 0} \approx X'$  and term this regression sampling.

Note that, in general, RMs can be seen as a special case of DMs, where setting  $T=1$  during the training only optimizes the single-step regression prediction from the source images (with only vacuum noise as additional input). We omit training dedicated RMs here, as we observed only negligible benefits over regression-sampled DMs.

5) *3D coherency in regression sampling*: As  $v_\theta$  operates in 2D, regression sampling lacks access to 3D information. Thus, to improve the performance of regression sampling, we aggregate the predictions of all three views. Additionally, 2.5D diffusion homogenizes the appearance of individual slices due to orthogonal denoising (Sec. III-B.1). For a similar effect for regression sampling, we propose to correct the individual slices  $\hat{X}_j$  that form the volumes via gamma corrections

$$\Gamma_{\theta_j}(\hat{X}_j) = (1 + a_j) \hat{X}_j^{(1+\gamma_j)} + c_j, \quad (10)$$

with a set of parameters  $\theta_j = \{a_j, \gamma_j, c_j\}$  for each slice  $\hat{X}_j$ . We then optimize the parameters  $\theta_j$  to minimize the intensity

differences between adjacent slices  $\hat{X}_j$  and  $\hat{X}_{j+1}$ :

$$\arg \min_{\{\theta_0, \dots, \theta_{N-1}\}} \frac{1}{N-1} \sum_{j=0}^{N-2} L_2(\Gamma_{\theta_j}(\hat{X}_j), \Gamma_{\theta_{j+1}}(\hat{X}_{j+1})) \quad (11)$$

### C. Datasets and preprocessing

We obtained a stratified set of 2233 participants of the RS [16], which were split into 1344 for training, 237 for validation, and 600 for testing. 52 additional participants with manual WMH annotation [14] constituted the WMH test set. MR acquisition was conducted at two sites using the same 3T scanner type and protocol [16]. We also tested on 82 *Mind-brain-body* study (MBB) participants for whom T1w, T2w, and 1 mm FLAIR images were available [55]. T1w and T2w were registered (RS: *mri\_coreg*, MBB: *bbregister*) to the FLAIR images and interpolated (cubic) to 1 mm with *FreeSurfer* (v7.4) [56], [57].

The IXI dataset (brain-development.org/ixi) contains T1w, T2w, and proton-density (PD) images from 577 participants (111 withheld for testing) acquired at three different sites equipped with 1.5 or 3T scanners from two vendors. We registered the T1w and PD to the T2w images with *mri\_coreg*. For BraTS, we utilized the training and validation data from the 2023 challenge [17], [43], [44], randomly selecting 200 cases from the pool of training cases added since the 2020 challenge to obtain a test set with reference tumor segmentation labels. The final models were trained on the remaining training cases combined with the validation set. The BraTS dataset includes data from various centers and protocols, and is provided as normalized and skull-stripped images resampled to a 1 mm resolution. We derived full-brain segmentation masks and, for all but the BraTS dataset, performed robust intensity normalization with *FastSurfer* (v2.2) [58], [59].

MRI-to-CT translation was performed in 15 participants (4 for testing) of the Gold Atlas [45], which provided co-registered CT, T1w, and T2w images. We created tissue masks based on intensity thresholds on the T1w images and excluded the upper and lower 5 slices due to decreased quality.

We defined the region-of-interest (ROI) for translation as the 3D bounding box of the tissue masks expanded by 5, 10, and 20 (axial, coronal, sagittal) voxels.

All participants gave informed consent to the respective studies.

### D. Implementation details

*YODA* is parametrized by a U-Net [10], [33] with 5 ResNet blocks (128/128/256/256/512 channels) in the en- and decoder, group normalization (group size 32), SiLU activation functions, and residual self-attention layers with time-step embedding (0/0/1/1/2 heads), resulting in 53M parameters. For our final RS model (Tab. I), we increase the size to 214M parameters. Source image conditioning is realized via channel-wise concatenation [9]. We use the linear [5] (default) and cosine noise schedules [60] with  $T = 1000$ .

We train *YODA* with an ADAM optimizer with a learning rate (LR) of  $10^{-4}$  (chosen from  $\{10^{-3}, 10^{-4}, 10^{-5}\}$ ), a batch

size of 96 (Gold atlas: 24), and track the parameters’ exponential moving average with a decay factor of 0.999 (from  $\{0, 0.99, 0.999, 0.9999\}$ ). To ensure a balanced training effort, we randomly sample the slicing plane and then a slice within the ROI. In total, we sample each volume 20k times, i.e. each slice, on average, 125 times. Training the larger model on the RS dataset requires ca. 30 GPU days (Nvidia V100s).

In line with our baseline methods, we omit skull-stripping for IXI. For training *YODA* on the RS, we reduce the weight of voxels outside the brain mask to a small  $\varepsilon = 0.01$ , which retains the skull for downstream uses while focusing on actual brain translation. As this is not possible for adversarial losses, we skull-strip the images for a fair comparison.

We perform slice homogenization following (11) for BraTS regression sampling by optimizing  $\theta_i$  with stochastic gradient descent (LR = 10). We exclude background voxels and add a small MSE penalty ( $\varepsilon = 0.01$ ) for  $\theta_i$  to the loss. The optimization converges within 2000 steps ( $<10$  seconds).

### E. Competing methods

We selected baseline methods based on relative performance, reproducibility, and availability of code. We considered ResViT [20] and dEa-GAN [21] as competing GANs, the adversarial DM *SynDiff* [25] and the DB *SelfRDB* [26] as competing DMs, and ALDM [27] as competing 3D LDM. All models were trained with the recommended hyperparameters. For the training, we adopted the same slice sampling scheme as *YODA* for all 2D methods (Sec. III-D). *SynDiff* was adapted for paired translation [25]. For *SelfRDB* we use the T2w or PD image as the DB prior and added the T1w as an additional conditioning. *ResViT* was implemented as a single-task model. For ALDM, we halved the size of the VQ-VAE to scale the model to our largest hardware (Nvidia A100-40GB).

### F. Metrics and statistical analyses

**Image Metrics:** To obtain the 3D SSIM and the PSNR, we applied the brain or pelvic tissue masks and cropped the images to the bounding box. The perceptual quality was evaluated with the FID [52] using a *ResNet-50* trained on *RadImageNet* [61] applied to axial slices.

To estimate the magnitude of noise ( $\hat{\sigma}$  in (3)) in synthetic images  $\hat{X}$ , we smooth the WM voxels (3D Gaussian blur, kernel size 5,  $\sigma_{\text{blur}} = 1.1$ ). The noise variance  $\hat{\sigma}_{\text{WM}}^2$  is then approximated via the deviations from the local mean intensity for WM voxels not adjacent to tissue boundaries.

**Downstream Metrics:** For WMH segmentation, we utilized the FLAIR-only version of *SHIVA-WMH* [62] after bias-field correction [63]. For glioma segmentation, we employed the winner of the 2020 BraTS challenge [64], [65]. In both tasks, we compared the results to the respective reference annotations. For full-brain segmentation from T2w images, we compared *SynthSeg* (v2.0) segmentations [66] with *FastSurfer* segmentation masks (obtained from T1w images). For bone and muscle segmentation from CT segmentation, we applied *TotalSegmentor* [67] relating segmentation from synthetic and acquired images. The performance was measured with the Dice score, the Hausdorff distance (HD, 95<sup>th</sup> percentile), and

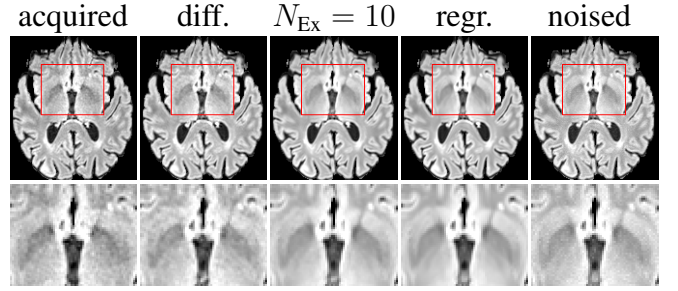


Fig. 1. FLAIR images generated by *YODA* with diffusion (diff.), ExpA ( $N_{\text{Ex}}=10$ ), regression (regr.) sampling, and noised regression images are compared to an acquired image (see also the supplementary video). Note that ExpA resembles regression sampling and achieves crisper edges but loses fine-grained details compared to diffusion sampling.

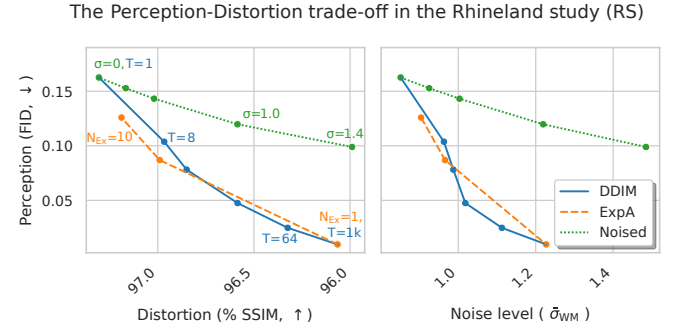


Fig. 2. Left: *YODA*’s perception-distortion trade-off [38] for diffusion ( $N_{\text{Ex}}=1, T=1k$ ), ExpA ( $N_{\text{Ex}}=4, 10$ ), DDIM ( $T \in \{64, 32, 16, 8\}$ ), regression ( $T=1$ ), and noised regression images is quantified using the FID and SSIM in the RS. Right: correlation of noise ( $\hat{\sigma}_{\text{WM}}$ ) and FID.

the absolute  $\log_2$  volume ratio (ALVR) [15].

As a tool-independent measure of WMH translation quality, we define the contrast-to-noise ratio (CNR) for each WMH (i.e. each labeled connected component) as

$$\text{CNR} = \frac{\mu^{\text{WMH}} - \mu^{\text{WM}}}{\sigma^{\text{WM}}}, \quad (12)$$

where  $\mu^{\text{WMH}}$  denotes mean WMH intensity, while  $\mu^{\text{WM}}$  and  $\sigma^{\text{WM}}$  denote mean and std. of isointense WM within a 3 mm distance from each WMH. We then take voxel-wise averages. We report all metrics as mean  $\pm$  std. The statistical analyses used non-parametric Wilcoxon signed-rank tests considering  $p < 0.05$  significant without multiple-comparison correction.

## IV. EXPERIMENTAL RESULTS

We tested *YODA* for MRI contrast translation in the RS (Tab. I, including assessing generalization to the external MBB dataset) and BraTS (Tab. II, left) for T1w, T2w  $\rightarrow$  FLAIR, on IXI for T1w, PD  $\rightarrow$  T2w (Tab. II, right), and on the pelvic Gold atlas dataset for MRI  $\rightarrow$  CT translation (Tab. III). Example images for brain MRI translation are provided in Fig. 3 and for pelvis translation in Fig. 5. First, we analyzed the impact of noise in *YODA*’s sampling methods on the assessed performance and then benchmarked *YODA* performance against competing methods. Finally, we demonstrated the benefits of *YODA* components and design choices in ablation studies.

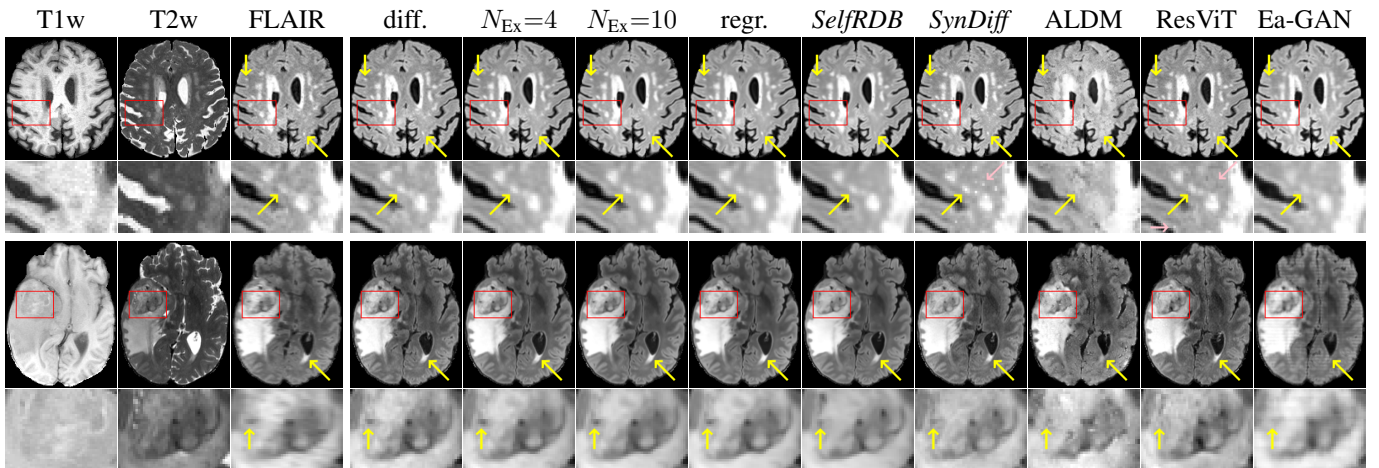


Fig. 3. Diffusion, ExpA, and regression sampling of *YODA* is demonstrated against competing methods for T1w,T2w  $\rightarrow$  FLAIR translation on random images of the RS (upper) and BraTS (lower). Note that all sampling methods of *YODA* allow for a more faithful translation of lesions while avoiding artifacts such as Salt-and-Pepper noise and other unrealistic textures. See also the supplementary video for additional translation results.

TABLE I

PERFORMANCE FOR RS-TRAINED BRAIN MRI TRANSLATION (T1w,T2w  $\rightarrow$  FLAIR) FOR IN- AND EXTERNAL (MBB) TEST SETS. \* AND  $\dagger$  MARK SIGNIFICANT ( $p < 0.05$ ) DIFFERENCES TO REGRESSION SAMPLING *YODA* AND TO WMH SEGMENTATION ON ACQUIRED IMAGES, RESPECTIVELY.

	required time	test set ( $n = 600$ )		MBB set ( $n = 82$ )		WMH test set ( $n = 52$ , manual reference)		
		SSIM (%), $\uparrow$	PSNR (dB), $\uparrow$	SSIM (%), $\uparrow$	PSNR (dB), $\uparrow$	Dice [62] (%), $\uparrow$	ALVR [62] ( $\downarrow$ )	CNR (%), $\uparrow$
<i>YODA</i> (regr.)	20 s	<b>97.31 <math>\pm</math> 0.90</b>	33.66 $\pm$ 1.95	93.25 $\pm$ 1.14	26.75 $\pm$ 1.19	<b>58.72 <math>\pm</math> 18.51</b>	<b>0.30 <math>\pm</math> 0.25<math>\dagger</math></b>	<b>3.54 <math>\pm</math> 0.51</b>
<i>YODA</i> ( $N_{\text{Ex}}=10$ )	2.5 h	97.19 $\pm$ 0.93*	<b>33.79 <math>\pm</math> 1.82*</b>	<b>93.27 <math>\pm</math> 1.16</b>	26.76 $\pm$ 1.22	58.48 $\pm$ 18.70* $\dagger$	<b>0.30 <math>\pm</math> 0.23<math>\dagger</math></b>	3.48 $\pm$ 0.49*
<i>YODA</i> ( $N_{\text{Ex}}=4$ )	1 h	96.99 $\pm$ 0.97*	33.57 $\pm$ 1.76*	93.14 $\pm$ 1.16*	26.70 $\pm$ 1.20*	58.21 $\pm$ 18.62* $\dagger$	0.31 $\pm$ 0.24 $\dagger$	3.42 $\pm$ 0.48* $\dagger$
<i>YODA</i> (diff.)	¼ h	96.07 $\pm$ 1.12*	32.66 $\pm$ 1.53*	92.46 $\pm$ 1.20*	26.42 $\pm$ 1.14*	56.12 $\pm$ 19.10* $\dagger$	0.37 $\pm$ 0.30* $\dagger$	3.18 $\pm$ 0.45* $\dagger$
<i>SelfRDB</i>	90 s	95.68 $\pm$ 1.10*	30.75 $\pm$ 1.43*	92.72 $\pm$ 1.17*	27.12 $\pm$ 1.37*	55.73 $\pm$ 21.12* $\dagger$	0.42 $\pm$ 0.36*	3.32 $\pm$ 0.66* $\dagger$
<i>SynDiff</i>	15 s	96.18 $\pm$ 1.06*	32.42 $\pm$ 1.57*	92.76 $\pm$ 1.24*	<b>27.32 <math>\pm</math> 1.49*</b>	55.65 $\pm$ 19.30* $\dagger$	0.45 $\pm$ 0.36*	3.27 $\pm$ 0.53* $\dagger$
ALDM	60 s	87.92 $\pm$ 1.39*	26.57 $\pm$ 2.15*	89.03 $\pm$ 1.86*	25.77 $\pm$ 1.66*	32.35 $\pm$ 22.86* $\dagger$	1.15 $\pm$ 0.89* $\dagger$	1.32 $\pm$ 0.57* $\dagger$
ResViT	10 s	94.72 $\pm$ 1.13*	30.52 $\pm$ 1.33*	90.15 $\pm$ 1.49*	25.66 $\pm$ 1.60*	54.04 $\pm$ 19.55* $\dagger$	0.50 $\pm$ 0.41*	2.96 $\pm$ 0.52* $\dagger$
Ea-GAN	5 s	95.76 $\pm$ 0.97*	31.45 $\pm$ 1.46*	92.14 $\pm$ 1.08*	26.79 $\pm$ 1.32	42.86 $\pm$ 20.29* $\dagger$	0.92 $\pm$ 0.66* $\dagger$	2.54 $\pm$ 0.54* $\dagger$
Acquired	4.5 min	100	-	100	-	59.44 $\pm$ 17.39	0.43 $\pm$ 0.34*	3.50 $\pm$ 0.39

### A. *YODA* sampling methods

To test the impact of the iterative refinement on *YODA*'s translation quality, we compared regression and diffusion sampling on the RS data and present additional generation examples in Fig. 1. We observe that diffusion sampling visually resembles the appearance of the acquired images. Regression sampling preserves key anatomical features (Fig. 1) – the GM/WM boundary, WMHs (Fig. 3), the outline of the pallidum – but omits many high-frequency features. To investigate whether iterative refinement during diffusion sampling adds relevant and systematic medical information or only imitates acquisition noise, we performed ExpA sampling, i.e. averaging the output of several ( $N_{\text{Ex}}=4$  or  $N_{\text{Ex}}=10$ ) diffusion trajectories. We observed a gradual loss of high-frequency details when increasing the  $N_{\text{Ex}}$  (see also the supplementary video), indicating that the effect of the iterative refinement is non-systematic. For  $N_{\text{Ex}}=10$ , the images are visually almost indistinguishable from the initial regression solution (SSIM: 99.73%, PSNR: 45.30 dB). The quantitative analysis of the image quality (Tab. I) showed that diffusion sampling impairs the assessed SSIM and PSNR in comparison to regression sampling for both the in- and external test sets, which we attribute to noise generation (Sec. III-A). In

turn, ExpA averages improved both metrics and, for  $N_{\text{Ex}}=10$ , performed mostly on par with the regression solution in both test sets in terms of SSIM, while the PSNR in the RS was slightly increased (Tab. I). However, we observed that ExpA sampling *YODA* improves the replication of systematic 3D low-frequency image intensity drifts (bias fields) due to the 3D synchronization in 2.5D diffusion sampling. Yet, this apparent advantage did not generalize to the external MBB dataset, as bias fields are MR protocol-specific.

To quantify the effect of noise on the assessed image quality, we used the std. in the WM ( $\sigma_{\text{WM}}$ ) to approximate the noise level of the generated images ( $\hat{\sigma}$  in (3)), interpolated between native diffusion ( $T = 1k$ ) and single-step regression sampling ( $T = 1$ ) by varying the number of time steps in DDIM sampling [68], and added Rician noise to the smooth regression images. We then assessed the distortion and the perceptual quality, presenting the results in Fig. 2. We observed that a higher number of DDIM steps or lower  $N_{\text{Ex}}$  improved the perceptual quality while inducing stronger distortion. Thus, these parameters steer the perception-distortion tradeoff [38]. Furthermore, we noted that the FID correlated with the estimated noise magnitude  $\sigma_{\text{WM}}$ , and that noising the smooth regression images gradually improved the FID.

To assess the actual medical information in synthetic FLAIR images, we evaluated the impact of the proposed sampling methods on the performance of the independent, externally trained *SHIVA*-WMH tool as compared to manual reference labels (Tab. I). Smoother images (higher  $N_{\text{Ex}}$  or from regression sampling) yielded improved performance over those from diffusion sampling. Regression images led to slightly lower Dice score ( $p = 0.082$ ), but higher derived volume correlation (ALVR,  $p < 10^{-3}$ ) than on acquired images (Tab. I). Note that for quality differences as close as reported here, the acquired-to-synthetic comparison is biased in favor of acquired images as the acquisition noise systematically affects both manual and *SHIVA*-WMH segmentations. To assess the suitability of *YODA*-generated images for WMH detection independent of segmentation tools, we also calculated the CNR (12) of WMHs. This confirmed that the contrast of WMHs is preserved in the regression images, whereas we noted slightly reduced WMH contrast for diffusion and ExpA-sampled images (Tab. I).

As a final assessment, we applied the internal RS WMH segmentation pipeline [14], [16] to the smooth regression images. As this pipeline was trained with image-label pairs of the RS WMH test, we only compared the derived volumes from inputting acquired vs. regression images in the larger, unannotated RS test set ( $n = 599$ , one removed due to a processing error). Despite the domain shift from noisy to smooth images, the pipeline remained robust and showed excellent agreement (ICC (3, 1): 0.982, 95% CI [0.98, 0.99]) with a near-perfect calibration and only a few outliers (Fig. 4).

**Confirmation in other datasets:** For BraTS and IXI datasets, we noted the same convergence of visual appearance for diffusion to regression sampling when increasing the  $N_{\text{Ex}}$  (Fig. 3) as observed in the RS. Also, we observed similar tendencies in terms of SSIM and PSNR, and for the performance of the respective downstream tasks (Tab. II). When assessing segmentation from *YODA*'s synthetic and acquired images, we measured significantly reduced performance for all sampling methods on BraTS, whereas the performance in IXI improved. In the MRI  $\rightarrow$  CT translation in the Gold atlas dataset (Fig. 5), major bones and muscles are translated faithfully. Yet, diffusion sampling leads to some inaccuracies in the outline of bones and hallucinations of the textures of inner organs. Conversely, regression sampling faithfully translates bones while still blurring the inner organs and generating artifacts. This indicates that rendering CTs is under-defined by the given MRI guidance alone. In the quantitative analysis

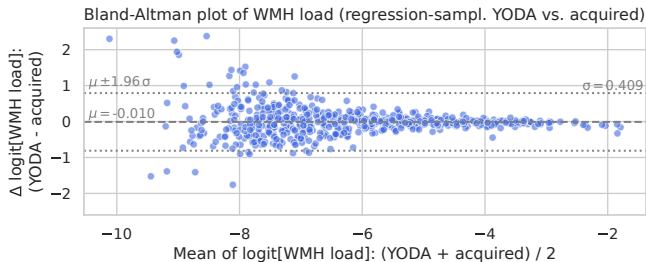


Fig. 4. Bland-Altman plot comparing logit-transformed WMH loads obtained from applying the RS WMH pipeline [14] to acquired or *YODA*-generated (regression sampling) images.

(Tab. III), we found a slightly increased performance of sampling with  $N_{\text{Ex}}=10$  over regression sampling in terms of PSNR and accuracy of the downstream task. As performance gains are marginal and the assessment is based on few ( $n = 4$ ) test cases, we still assume the performance of diffusion and regression to be similar.

## B. Performance benchmarking

We then compared *YODA* against the competing baseline methods. On the RS data (Tab. I), regression sampling of *YODA* significantly outperformed all other methods both w.r.t. the image quality and downstream WMH segmentation, and achieved superior image quality in the external MBB test set. When analyzing the RS synthesis results (Fig. 3, see also the supplementary video), we noted that most reference methods strive to imitate realistic images, but several artifacts can be observed such as hallucinated WMHs (*SynDiff*) and salt-and-pepper noise (*SynDiff*, ResViT). *SelfRDB* produces relatively smooth images, likely owing to its self-consistent sampling procedure, while ALDM is not able to reproduce smaller lesions, which we attribute to missing representations in the compressed latent space. Furthermore, our analysis underlines that pure intensity-based performance metrics are a faulty indicator of WMH translation quality, as e.g. *Ea-GAN* achieved competitive SSIM and PSNR, but WMH translation was poor (Tab. I). Note that runtime of regression sampling *YODA* is competitive and even faster than FLAIR acquisition. When benchmarking on the more heterogeneous and lower-quality BraTS dataset (Tab. II, left), regression sampling of *YODA* achieved significantly better images than all competing methods in terms of PSNR, SSIM, and downstream glioma segmentation. Similar results were obtained in the IXI dataset (Tab. II, right), where *YODA* significantly outperformed all competing methods in SSIM and PSNR. In the full-brain segmentation conducted from the synthetic images, *YODA*'s images were significantly better than all competing methods except *Ea-GAN* in at least either the Dice score or the HD. In the MRI  $\rightarrow$  CT task on the small pelvic dataset, regression sampling of *YODA* outperformed all competing methods by  $\geq 1.6\%$  SSIM and  $> 0.5$  dB PSNR, and improved by  $> 0.6\%$  Dice, 0.09 mm HD over the best competing method. Note that, for all methods, the translation of inner organs was rather poor and included either texture hallucination (ResViT, diffusion-sampling *YODA*) or an over-smooth image appearance (*SelfRDB*, *SynDiff*, Exp and regression sampling *YODA*, Fig. 5).

## C. Ablation of YODA components

1) **2.5D diffusion:** To enable coherent 3D sampling of 2D DMs, we introduced 2.5D diffusion. Single-slice and single-plane denoising results in slicing artifacts due to diverging sampling trajectories in adjacent slices, which are prevented by multi-slice inputs and orthogonal denoising (Fig. 6). Both 2.5D modifications individually resulted in significantly improved SSIM and PSNR, while combining both led to additional improvements (Tab. IV). Multi-slice inputs also slightly improved regression sampling.

TABLE II

PERFORMANCE FOR BRAIN MRI TRANSLATION IN THE BRATS (T1w,T2w → FLAIR) AND IXI (T1w,PD → T2w) DATASETS. \* AND † MARK SIGNIFICANT DIFFERENCES TO REGRESSION SAMPLING YODA AND TO SEGMENTATION (SEGM.) ON ACQUIRED IMAGES, RESPECTIVELY.

	BraTS dataset ( $n = 200$ , downstream glioma segm. [65])				IXI dataset ( $n = 111$ , downstream full-brain segm. [66])			
	SSIM (% , †)	PSNR (dB , †)	Dice (% , †)	HD (mm , †)	SSIM (% , †)	PSNR (dB , †)	Dice (% , †)	HD (mm , †)
<i>YODA</i> (regr.)	<b>90.87 ± 5.45</b>	<b>27.23 ± 3.19</b>	<b>83.34 ± 14.81</b> †	<b>5.13 ± 5.25</b> †	<b>98.26 ± 0.73</b>	<b>37.40 ± 2.11</b>	<b>73.54 ± 1.81</b> †	<b>2.71 ± 0.63</b> †
<i>YODA</i> ( $N_{Ex}=10$ )	90.44 ± 5.57*	26.91 ± 3.17*	83.33 ± 14.79†	5.16 ± 5.13†	98.18 ± 0.76*	37.23 ± 2.07*	73.51 ± 1.79*†	2.72 ± 0.63†
<i>YODA</i> ( $N_{Ex}=4$ )	90.03 ± 5.56*	26.79 ± 3.11*	83.31 ± 14.79†	5.17 ± 5.16†	98.03 ± 0.81*	36.89 ± 2.03*	73.50 ± 1.79*†	<b>2.71 ± 0.63</b> †
<i>YODA</i> (diff.)	88.22 ± 5.53*	26.21 ± 2.84*	83.17 ± 14.87†	5.17 ± 5.12*†	97.29 ± 1.04*	35.47 ± 1.89*	73.39 ± 1.74*†	2.72 ± 0.62*
<i>SelfRDB</i>	88.26 ± 5.45*	25.74 ± 2.66*	82.29 ± 16.31*†	5.32 ± 5.16*†	97.79 ± 0.86*	35.38 ± 1.85*	73.46 ± 1.72*†	2.72 ± 0.61
<i>SynDiff</i>	86.56 ± 5.65*	25.19 ± 2.47*	82.13 ± 16.06*†	5.31 ± 5.04*†	97.38 ± 0.99*	34.69 ± 1.78*	73.00 ± 1.56*†	2.82 ± 0.46*†
ALDM	77.58 ± 6.08*	21.09 ± 2.55*	80.31 ± 16.33*†	5.77 ± 5.32*†	86.70 ± 1.96*	25.10 ± 0.97*	62.13 ± 13.13*†	4.70 ± 3.43*†
ResViT	83.35 ± 5.29*	24.14 ± 2.05*	82.43 ± 15.17*†	5.30 ± 5.22*†	96.64 ± 1.21*	32.82 ± 1.98*	73.51 ± 1.77†	2.72 ± 0.55*
Ea-GAN	86.24 ± 5.03*	25.00 ± 2.21*	82.14 ± 16.23*†	5.41 ± 5.11*†	96.69 ± 1.15*	31.91 ± 1.66*	73.50 ± 1.83†	<b>2.71 ± 0.63</b>
Acquired	100	-	84.86 ± 15.14	4.90 ± 5.13	100	-	73.28 ± 1.81	2.73 ± 0.63

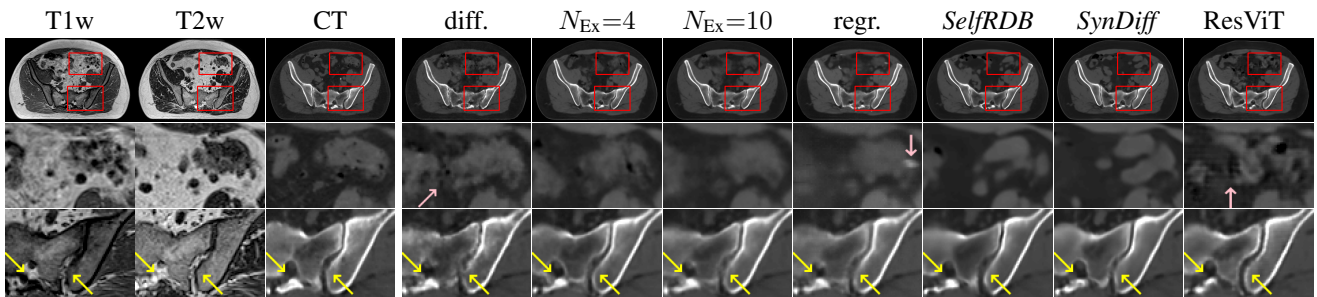


Fig. 5. *YODA* is demonstrated against competing methods for MRI → CT translation on the Gold atlas pelvis dataset on a random example. Diffusion sampling *YODA* results in hallucinated organ shapes and textures that smoothen out and disappear when increasing the  $N_{Ex}$  in Exp sampling or when using regression sampling. Regression sampling creates some artifacts. Note that, for all methods, the translation quality for inner organs is rather poor, whereas bone and muscle translation is reliable.

TABLE III

PERFORMANCE FOR MRI → CT TRANSLATION IN THE GOLD ATLAS.

	Quality metrics		Bone & muscle segm. [67]	
	SSIM (% , †)	PSNR (dB , †)	Dice (% , †)	HD (mm , †)
<i>YODA</i> (regr.)	89.47 ± 2.01	<b>25.46 ± 1.41</b>	94.40 ± 1.23	2.01 ± 0.41
<i>YODA</i> ( $N_{Ex}=10$ )	<b>89.64 ± 1.96</b>	25.32 ± 1.28	<b>94.82 ± 1.19</b>	<b>1.92 ± 0.41</b>
<i>YODA</i> ( $N_{Ex}=4$ )	88.74 ± 1.82	25.12 ± 1.28	94.37 ± 0.99	2.00 ± 0.33
<i>YODA</i> (diff.)	87.67 ± 1.76	25.00 ± 1.24	94.32 ± 0.91	2.01 ± 0.31
<i>SelfRDB</i>	87.87 ± 1.29	24.91 ± 1.37	92.92 ± 1.28	2.29 ± 0.19
<i>SynDiff</i>	86.98 ± 1.51	24.54 ± 1.08	93.76 ± 1.03	2.10 ± 0.31
ResViT	85.16 ± 3.87	24.12 ± 1.39	93.57 ± 2.24	2.10 ± 0.56

TABLE IV

ABLATION OF MULTI-SLICE INPUT (MS.) AND ORTHOGONAL DENOISING (OD.) ON THE RS DATASET. \* SIGNIFICANT DIFFERENCE TO A SINGLE-PLANE AND SINGLE-SLICE MODEL.

sampling	ms.	od.	SSIM (% , †)	PSNR (dB , †)
diff.	✓	✓	<b>95.92 ± 1.34*</b>	<b>33.13 ± 1.33*</b>
	✓	✗	95.86 ± 1.30*	32.88 ± 1.24*
	✗	✓	95.85 ± 1.31*	33.09 ± 1.31*
	✗	✗	95.27 ± 1.35	32.23 ± 1.16
regr.	✓	-	<b>97.12 ± 1.12</b>	<b>34.29 ± 1.51</b>
	✗	-	97.11 ± 1.13	34.23 ± 1.45

2) *Noise schedule*: We exchanged *YODA*'s default linear for a cosine noise schedule, which shifts the diffusion process towards higher SNRs. For both diffusion and regression sampling, this significantly decreased SSIM and PSNR, whereas the FID improved (Tab. V), i.e. perceptual quality is traded for more severe distortion. We attribute impaired regression

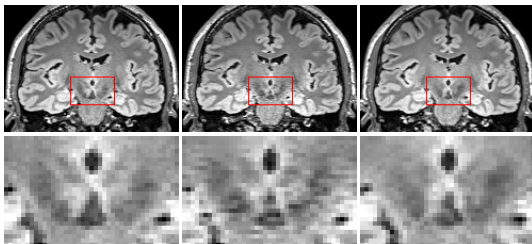


Fig. 6. Left to right: Acquired RS image, and diffusion-sampled images from 2D or 2.5D *YODA* versions, respectively.

quality to reduced training effort at low SNRs, i.e. image translation without meaningful diffusion priors. Nevertheless, both schedules lead to similar image quality under ExpA sampling, which implies that the cosine schedule simply shifts the translation towards higher SNRs without impacting the overall translation capabilities. Preferring the computationally cheaper regression solution, we disregarded the cosine schedule.

Based on the quality and stability of the predicted images  $\hat{X}_{t \rightarrow 0}$  at early diffusion steps ( $t \gg 0$ , i.e. low SNR) when using the linear schedule, we adopted a truncated sampling scheme skipping the first 3/4 steps to spare compute. This does not have any measurable impact on image quality in comparison to running the full reverse process (Tab. V).

3) *Training target*: To study the effect of the prediction target on the sample quality, the velocity ( $v$ ) was exchanged for simple noise ( $\epsilon$ ) or image ( $X_0$ ) prediction (Tab. VI). Both

TABLE V

ABLATION OF NOISE SCHEDULES (COSINE VS. TRUNCATED AND FULL LINEAR) ON THE RS DATASET. \* SIGNIFICANT DIFFERENCES TO THE DEFAULT SETTING (TRUNCATED LINEAR SCHEDULE).

sampl.	schedule	SSIM (% , $\uparrow$ )	PSNR (dB, $\uparrow$ )	FID ( $\downarrow$ )
diff.	lin. (truncated)	<b>95.92 <math>\pm</math> 1.34</b>	<b>33.14 <math>\pm</math> 1.32</b>	0.0106
	lin. (full)	<b>95.92 <math>\pm</math> 1.34</b>	33.13 $\pm$ 1.33	0.0105
	cos.	95.83 $\pm$ 1.37	33.02 $\pm$ 1.35	<b>0.0076</b>
ExpA ( $N_{\text{Ex}}=4$ )	lin. (truncated)	<b>96.92 <math>\pm</math> 1.18</b>	<b>34.34 <math>\pm</math> 1.49</b>	0.1194
	cos.	<b>96.92 <math>\pm</math> 1.19</b>	34.29 $\pm$ 1.53	<b>0.1148</b>
regr.	lin.	<b>97.12 <math>\pm</math> 1.12</b>	<b>34.29 <math>\pm</math> 1.51</b>	0.2053
	cos.	96.76 $\pm$ 1.12*	33.85 $\pm$ 1.46*	<b>0.1754</b>

TABLE VI

ABLATION OF VELOCITY ( $v$ ), NOISE ( $\epsilon$ ), AND IMAGE ( $X_0$ ) PREDICTION ON THE RS DATASET. \* SIGNIFICANT DIFFERENCES TO  $v$ - PREDICTION.

sampl.	target	SSIM (% , $\uparrow$ )	PSNR (dB, $\uparrow$ )
diff.	$v$	<b>95.97 <math>\pm</math> 1.13</b>	<b>33.16 <math>\pm</math> 1.28</b>
	$\epsilon$	95.67 $\pm$ 1.21*	32.79 $\pm$ 1.33*
	$X_0$	94.94 $\pm$ 1.15*	31.91 $\pm$ 1.09*
ExpA ( $N_{\text{Ex}}=4$ )	$v$	<b>96.97 <math>\pm</math> 0.96</b>	<b>34.36 <math>\pm</math> 1.44</b>
	$\epsilon$	96.77 $\pm$ 0.99*	34.07 $\pm$ 1.44*
	$X_0$	96.23 $\pm$ 0.98*	33.14 $\pm$ 1.22*
regr.	$v$	<b>97.16 <math>\pm</math> 0.90</b>	<b>34.31 <math>\pm</math> 1.47</b>
	$X_0$	96.89 $\pm$ 0.91*	33.93 $\pm$ 1.35*

parametrization alternatives result in significantly reduced performance in all sampling methods. Note that regression sampling is not possible for  $\epsilon$ -prediction.

## V. DISCUSSION

In this work, we systematically assessed the presumed benefits of DMs in MIT. Whereas we confirmed that the iterative refinement in DM sampling indeed improves the perceptual quality, we noted that this implies the replication of inherent and undesired acquisition noise. Moreover, we showed that the perceptual quality can simply be improved by adding noise to smooth images, which implies destroying the contained information. We obtained the same results when exchanging the FID for the average paired cosine or  $L_2$  feature similarity (not shown), which is supposed to be a more semantic measure [38]. This highlights the inherent ill-posing of perceptual metrics rating realism (i.e. the ability to imitate real images  $X$ ) rather than the contained medical information (i.e. correctly predict noise-free images  $X'$ ). While the perception-distortion tradeoff of artificially noising the regression images was worse than for native DM sampling, noise realism can likely be improved by applying more complicated noise patterns, e.g. by simulating noise of accelerated MRI acquisition [37]. Furthermore, we noted that both DDIM sampling and ExpA averages gradually trade in perceptual quality to reduce distortion. Thus, claimed improvements of image quality due to accelerated DM sampling [25], [28], [31] or implicit ExpA averages [29], [32] might simply result from image smoothing and noise suppression. Our regression DM sampling hereby constitutes the most resolute optimization for reducing distortion over improving the perceptual quality. In turn, we found no evidence for noise benefiting automated

downstream tasks and, moreover, the smooth regression images achieved better downstream performance than the more realistic diffusion images across all MRI translation tasks. This even holds when domain shifts can be ruled out by the training strategy [66] or data [14]. Human experts might also be unfamiliar with the smooth, noise-free, and, thus rather unrealistic images. However, noise suppression and, thus, improved contrast could also help in manual downstream tasks or visual inspection. Thus, applying RMs is supported by optimizing the extractable medical information.

Using smooth regression rather than noisy acquired images achieved at least comparable accuracy in downstream applications, except for glioma segmentation in BraTS. Yet, this dataset is of particularly low quality, especially w.r.t. image co-registration [23], which impairs information richness in the source images and induces spatial misalignment of segmentation maps. While we noted reduced quality metrics of the RS-trained *YODA* applied to the external MBB data, we partly attribute this to a mismatch of the respective MRI protocols, i.e. RS-like synthetic images are compared to distinctive MBB FLAIR images. Therefore, we still assume that the translation generalizes to external source images. Note that *YODA* in combination with established WMH tools [14], [62] – to the best of our knowledge for the first time – also allows for accurate WMH segmentation without FLAIR images.

For brain MRI translation, diffusion sampling at  $N_{\text{Ex}}=10$  performed slightly inferior to regression sampling in most MIT tasks, which we attribute to noise remnants. Yet, extrapolating to higher  $N_{\text{Ex}}$ , we assume that ExpA-averaged diffusion and regression sampling are practically equivalent. For  $N_{\text{Ex}} \gg 10$ , diffusion sampling might show small benefits e.g. in slightly improved generalization to unseen input data, as foreshadowed by results on the MBB. However, it would come at the cost of a couple of thousand times higher  $N_{\text{FE}}$ , which is computationally intractable and, therefore, irrelevant in practice. Hence, our results question the presumed superiority of DMs in MIT, especially when considering critical downstream evaluations. We attribute the popularity of these perceptual models to adapting them from the natural image domain without accounting for different requirements in MIT, which might be exacerbated by innovation biases [69]. Overall, our findings call for a thorough evaluation of new methods. The generated medical information should also be validated with relevant downstream tasks like segmenting lesions to avoid biases from noise replication and image appearance, in addition to considering simple RM baselines.

## REFERENCES

- [1] I. Goodfellow *et al.*, “Generative adversarial nets,” in *NeurIPS*, 2014.
- [2] P. Isola, J.-Y. Zhu, T. Zhou, and A. A. Efros, “Image-to-image translation with conditional adversarial networks,” in *CVPR*, 2017.
- [3] J. Sohl-Dickstein, E. Weiss, N. Maheswaranathan, and S. Ganguli, “Deep unsupervised learning using nonequilibrium thermodynamics,” in *ICML*, 2015.
- [4] Y. Song, J. Sohl-Dickstein, D. P. Kingma, A. Kumar, S. Ermon, and B. Poole, “Score-based generative modeling through stochastic differential equations,” in *ICLR*, 2021.
- [5] J. Ho, A. Jain, and P. Abbeel, “Denoising diffusion probabilistic models,” in *NeurIPS*, 2020.
- [6] C. Ledig *et al.*, “Photo-realistic single image super-resolution using a generative adversarial network,” in *CVPR*, 2017.

- [7] T. Karras, S. Laine, M. Aittala, J. Hellsten, J. Lehtinen, and T. Aila, "Analyzing and improving the image quality of stylegan," in *ICLR*, 2020.
- [8] P. Dhariwal and A. Nichol, "Diffusion models beat gans on image synthesis," in *NeurIPS*, 2021.
- [9] C. Saharia *et al.*, "Image super-resolution via iterative refinement," *IEEE PAMI*, vol. 45, no. 4, pp. 4713–4726, 2022.
- [10] R. Rombach, A. Blattmann, D. Lorenz, P. Esser, and B. Ommer, "High-resolution image synthesis with latent diffusion models," in *CVPR*, 2022.
- [11] S. Kazemini *et al.*, "Gans for medical image analysis," *J. Med. Artif. Intell.*, vol. 109, p. 101938, 2020.
- [12] A. Kazerouni *et al.*, "Diffusion models in medical imaging: A comprehensive survey," *MedIA*, vol. 88, p. 102846, 2023.
- [13] J. M. Wardlaw *et al.*, "Neuroimaging standards for research into small vessel disease and its contribution to ageing and neurodegeneration," *Lancet Neurol.*, vol. 12, no. 8, pp. 822–838, 2013.
- [14] V. Lohner *et al.*, "Relation between sex, menopause, and white matter hyperintensities: the rhineland study," *Neurology*, vol. 99, no. 9, pp. e935–e943, 2022.
- [15] H. J. Kuijf *et al.*, "Standardized assessment of automatic segmentation of white matter hyperintensities and results of the wmh segmentation challenge," *IEEE T-MI*, vol. 38, no. 11, pp. 2556–2568, 2019.
- [16] A. Koch *et al.*, "Versatile mri acquisition and processing protocol for population-based neuroimaging," *Nature Protocols*, pp. 1–23, 2024.
- [17] B. H. Menze *et al.*, "The multimodal brain tumor image segmentation benchmark (brats)," *IEEE T-MI*, vol. 34, no. 10, pp. 1993–2024, 2014.
- [18] M. F. Glasser *et al.*, "The human connectome project's neuroimaging approach," *Nature neuroscience*, vol. 19, no. 9, pp. 1175–1187, 2016.
- [19] S. U. Dar, M. Yurt, L. Karacan, A. Erdem, E. Erdem, and T. Çukur, "Image synthesis in multi-contrast mri with conditional generative adversarial networks."
- [20] O. Dalmaz, M. Yurt, and T. Çukur, "Resvit: residual vision transformers for multimodal medical image synthesis," *IEEE T-MI*, vol. 41, no. 10, pp. 2598–2614, 2022.
- [21] B. Yu, L. Zhou, L. Wang, Y. Shi, J. Fripp, and P. Bourgeat, "Ea-gans: edge-aware generative adversarial networks for cross-modality mr image synthesis," *IEEE T-MI*, vol. 38, no. 7, pp. 1750–1762, 2019.
- [22] J. Benzakoun *et al.*, "Synthetic flair as a substitute for flair sequence in acute ischemic stroke," *Radiology*, vol. 303, no. 1, pp. 153–159, 2022.
- [23] L. Kong, C. Lian, D. Huang, z. li, Y. Hu, and Q. Zhou, "Breaking the dilemma of medical image-to-image translation," *NeurIPS*, 2021.
- [24] Y. Zhang, C. Peng, Q. Wang, D. Song, K. Li, and S. K. Zhou, "Unified multi-modal image synthesis for missing modality imputation," *IEEE T-MI*, vol. 44, no. 1, pp. 4–18, 2025.
- [25] M. Özbey *et al.*, "Unsupervised medical image translation with adversarial diffusion models," *IEEE T-MI*, vol. 42, no. 12, pp. 3524–3539, 2023.
- [26] F. Arslan, B. Kabas, O. Dalmaz, M. Ozbey, and T. Çukur, "Self-consistent recursive diffusion bridge for medical image translation," *arXiv:2405.06789*, 2024.
- [27] J. Kim and H. Park, "Adaptive latent diffusion model for 3d medical image to image translation: Multi-modal magnetic resonance imaging study," in *IEEE WACV*, 2024.
- [28] Z. Xing *et al.*, "Cross-conditioned diffusion model for medical image to image translation," in *MICCAI*, 2024.
- [29] K. Choo, Y. Jun, M. Yun, and S. J. Hwang, "Slice-consistent 3d volumetric brain ct-to-mri translation with 2d brownian bridge diffusion model," in *MICCAI*, 2024.
- [30] X. Meng, K. Sun, J. Xu, X. He, and D. Shen, "Multi-modal modality-masked diffusion network for brain mri synthesis with random modality missing," *IEEE T-MI*, vol. 43, no. 7, pp. 2587–2598, 2024.
- [31] H. Jiang *et al.*, "Fast denoising diffusion probabilistic models for medical image-to-image generation," *arXiv:2405.14802*, 2024.
- [32] Y. Zhou *et al.*, "Cascaded multi-path shortcut diffusion model for medical image translation," *MedIA*, vol. 98, p. 103300, 2024.
- [33] W. H. Pinaya *et al.*, "Generative ai for medical imaging: extending the monai framework," *arXiv:2307.15208*, 2023.
- [34] H. Chung, E. S. Lee, and J. C. Ye, "Mr image denoising and super-resolution using regularized reverse diffusion," *IEEE T-MI*, vol. 42, no. 4, pp. 922–934, 2022.
- [35] C. J. Holmes, R. Hoge, L. Collins, R. Woods, A. W. Toga, and A. C. Evans, "Enhancement of mr images using registration for signal averaging," *JCAT*, vol. 22, no. 2, pp. 324–333, 1998.
- [36] H. Gudbjartsson and S. Patz, "The rician distribution of noisy mri data," *Magn. Reson. Med.*, vol. 34, no. 6, pp. 910–914, 1995.
- [37] S. Aja-Fernández and A. Tristán-Vega, "A review on statistical noise models for magnetic resonance imaging," *Tech. Rep.*, 2013.
- [38] Y. Blau and T. Michaeli, "The perception-distortion tradeoff," in *CVPR*, 2018.
- [39] J. Lehtinen *et al.*, "Noise2noise: Learning image restoration without clean data," in *ICML*, 2018.
- [40] A. F. Osman and N. M. Tamam, "Deep learning-based convolutional neural network for intramodality brain mri synthesis," *Med. Phys.*, vol. 23, no. 4, p. e13530, 2022.
- [41] C. Saharia *et al.*, "Palette: Image-to-image diffusion models," in *ACM SIGGRAPH*, 2022.
- [42] D. Watson, W. Chan, R. Brualla, J. Ho, A. Tagliasacchi, and M. Norouzi, "Novel view synthesis with diffusion models," in *ICLR*, 2023.
- [43] U. Baid *et al.*, "The rsna-asnr-miccai brats 2021 benchmark on brain tumor segmentation and radiogenomic classification," *arXiv:2107.02314*, 2021.
- [44] S. Bakas *et al.*, "Advancing the cancer genome atlas glioma mri collections with expert segmentation labels and radiomic features," *Sci. Data*, vol. 4, no. 1, pp. 1–13, 2017.
- [45] T. Nyholm *et al.*, "Mr and ct data with multiobserver delineations of organs in the pelvic area," *Med. Phys.*, vol. 45, pp. 1295–1300, 2018.
- [46] G.-H. Liu, A. Vahdat, D.-A. Huang, E. A. Theodorou, W. Nie, and A. Anandkumar, "I2sb: Image-to-image schrödinger bridge," *arXiv:2302.05872*, 2023.
- [47] B. Li, K. Xue, B. Liu, and Y.-K. Lai, "Bbmd: Image-to-image translation with brownian bridge diffusion models," in *IEEE CVPR*, 2023.
- [48] S. Pan *et al.*, "Cycle-guided denoising diffusion probability model for 3d cross-modality mri synthesis," *arXiv:2305.00042*, 2023.
- [49] W. Pinaya *et al.*, "Brain imaging generation with latent diffusion models," in *MICCAI Workshop on Deep Generative Models*, 2022.
- [50] L. Jiang, Y. Mao, X. Wang, X. Chen, and C. Li, "Cola-diff: Conditional latent diffusion model for multi-modal mri synthesis," in *MICCAI*, 2023.
- [51] W. Wei *et al.*, "Fluid-attenuated inversion recovery mri synthesis from multisequence mri using three-dimensional fully convolutional networks for multiple sclerosis," *J. Med. Imaging*, vol. 6, no. 1, 2019.
- [52] M. Heusel, H. Ramsauer, T. Unterthiner, B. Nessler, and S. Hochreiter, "Gans trained by a two time-scale update rule converge to a local nash equilibrium," in *NeurIPS*, 2017.
- [53] L. Pfaff *et al.*, "No-new-denoiser: A critical analysis of diffusion models for medical image denoising," in *MICCAI*, 2024.
- [54] T. Salimans and J. Ho, "Progressive distillation for fast sampling of diffusion models," *arXiv:2202.00512*, 2022.
- [55] A. Babayan *et al.*, "A mind-brain-body dataset of mri, eeg, cognition, emotion, and peripheral physiology in young and old adults," *Sci. Data*, vol. 6, no. 1, pp. 1–21, 2019.
- [56] B. Fischl, "Freesurfer," *NeuroImage*, vol. 62, no. 2, pp. 774–781, 2012.
- [57] D. N. Greve and B. Fischl, "Accurate and robust brain image alignment using boundary-based registration," *NeuroImage*, vol. 48, no. 1, pp. 63–72, 2009.
- [58] L. Henschel, S. Conjeti, S. Estrada, K. Diers, B. Fischl, and M. Reuter, "Fastsurfer - a fast and accurate deep learning based neuroimaging pipeline," *NeuroImage*, vol. 219, p. 117012, 2020.
- [59] L. Henschel, D. Kügler, and M. Reuter, "Fastsurfervinn: Building resolution-independence into deep learning segmentation methods—a solution for highres brain mri," *NeuroImage*, vol. 251, p. 118933, 2022.
- [60] A. Q. Nichol and P. Dhariwal, "Improved denoising diffusion probabilistic models," in *ICML*. PMLR, 2021, pp. 8162–8171.
- [61] X. Mei *et al.*, "Radimagenet: an open radiologic deep learning research dataset for effective transfer learning," *Radiol.: Artif. Int.*, vol. 4, no. 5, p. e210315, 2022.
- [62] A. Tsuchida, P. Boutinaud, V. Verrecchia, C. Tzourio, S. Debette, and M. Joliot, "Early detection of white matter hyperintensities using shivawmh detector," *Human Brain Mapping*, vol. 45, no. 1, p. e26548, 2024.
- [63] N. J. Tustison *et al.*, "N4itk: improved n3 bias correction," *IEEE T-MI*, vol. 29, no. 6, pp. 1310–1320, 2010.
- [64] F. Isensee, P. F. Jaeger, S. A. Kohl, J. Petersen, and K. H. Maier-Hein, "nnu-net: a self-configuring method for deep learning-based biomedical image segmentation," *Nat. methods*, vol. 18, no. 2, pp. 203–211, 2021.
- [65] F. Isensee, P. F. Jäger, P. M. Full, P. Vollmuth, and K. H. Maier-Hein, "nnu-net for brain tumor segmentation," in *MICCAI*, 2021.
- [66] B. Billot *et al.*, "Synthseg: Segmentation of brain mri scans of any contrast and resolution without retraining," *MedIA*, vol. 86, p. 102789, 2023.
- [67] J. Wasserthal *et al.*, "Totalsegmentator: robust segmentation of 104 anatomic structures in ct images," *Radiol.: Artif. Int.*, vol. 5, no. 5, 2023.
- [68] J. Song, C. Meng, and S. Ermon, "Denoising diffusion implicit models," in *ICLR*, 2021.
- [69] F. Isensee *et al.*, "nnu-net revisited: A call for rigorous validation in 3d medical image segmentation," in *MICCAI*, 2024.